First-principles investigation of electronic, mechanical and thermoelectric properties of graphene-like XBi (X = Si, Ge, Sn) monolayers

PCCP

ROYAL SOCIETY OF CHEMISTRY

ARTICLE TYPE

Cite this: DOI: 10.1039/xxxxxxxxxx

First-Principles investigation of Electronic, Mechanical and Thermoelectric Properties of Graphene-Like XBi (X=Si, Ge, Sn) monolayers

Asadollah Bafekry[1,2†], Mehmet Yagmurcukardes[3,4], Berna Akgenc[5], Mitra Ghergherehchi[6]

Received Date
Accepted Date

DOI: 10.1039/xxxxxxxxxx

www.rsc.org/journalname

Research progress on single-layer group III monochalcogenides have been increasing rapidly owing to their interesting physics. Herein, we investigate the stability and intrinsic properties of single-layer XBi (X=Ge, Si, or Sn) by using density functional theory calculations. Phonon band dispersion calculations and *ab-initio* molecular dynamics simulations reveal the dynamical and thermal stability of considered monolayers. Raman spectra calculations indicate the existence of 5 Raman active phonon modes 3 of which are prominent and can be observed in a possible Raman measurement. Electronic band structures of the XBi single-layers investigated with and without spin-orbit coupling effects (SOC). Our results show that XBi single-layers show semiconducting property with the narrow band gap values without SOC. However only the single-layer SiBi is an indirect band gap semiconductor while GeBi and SnBi exhibit metallic behaviors by adding spin-orbit coupling effects. In addition, the calculated linear-elastic parameters indicate the soft nature of investigated monolayers. Moreover, our results for the thermoelectric properties of single-layer XBi reveal that SiBi is a good thermoelectric material with increasing temperature. Overall, it is proposed that single-layer XBi structures can be alternative, stable 2D single-layers with their varying electronic and thermoelectric properties.

1 Introduction

The tremendous interests toward two dimensional (2D) materials was initiated by the graphene[1–3] exceptional physics. Other famous 2D materials include Xenes (X=Si, Ge, Sn, P, B, and so on)[4–7] and transition metal dichalcogenides (TMDs)[8], has shown outstanding physical features to design advanced nanodevices[9,10]. Particularity, the electronic bands of graphene yield Dirac cones in the vicinity of Fermi level, resulting in high carrier mobilities[11], superior mechanical and thermal conduction properties[12], wide band absorption[13], and other exceptional physical/chemical features. However, semi-metallic form of graphene has limited functionality in the semiconductor technology[14]. In view of this, the effort of searching stable free-standing atomic layers of semiconducting materials continuing to look for a new category of 2D material class[15–25].

Very recently, bismuth-based 2D materials have attracted remarkable interest due to their unique properties.[26,27] Bi shows very interesting features highly appealing for energy related applications. In fact, the electronic features of Bi-based nanomembranes can be easily modified via introduction of distinct anions and cations into the layered structure and the band gap can be tuned from 0.3 eV (near infrared absorption range) to 3.6 eV (ultraviolet absorption range)[28,29]. Moreover, Bi-based nanosheets belong to the anisotropic *p* and *s-p* hybridization which induces remarkably dispersed electronic structure[30]. Feng et al. summarized reports on the different strategies for using as the highly efficient visible-light photocatalysts by modifying electronic band structure with anisotropic *p* and *s-p* hybridization states[31]. They showed that highly dispersed electronic structure of Bi-layered components not only decreases the effective mass of photoexcited charge carriers and consequently enhance mobility, but also improve the charge separation and transmission efficiency in photoexcitation process, highly desirable for the employment in so-

[1] *Department of Radiation Application, Shahid Beheshti University, Tehran, Iran. E-mail: bafekry.asad@gmail.com*
[2] *Department of Physics, University of Antwerp, Groenenborgerlaan 171, B-2020 Antwerp, Belgium.*
[3] *NANOlab Center of Excellence, Groenenborgerlaan 171, B-2020 Antwerp, Belgium.*
[4] *Department of Photonics, Izmir Institute of Technology, 35430 Izmir, Turkey.*
[5] *Department of Physics, Kirklareli University, Kirklareli, 39100, Turkey.*
[6] *Department of Electrical and Computer Engineering, Sungkyunkwan University, 16419 Suwon, Korea.*
[7] *Chair of Computational Science and Simulation Technology, Institute of Photonics, Department of Mathematics and Physics, Leibniz Universitt Hannover, Appelstrasse 11,30167 Hannover, Germany.*
† *To whom correspondence should be addressed. Email: bafekry.asad@gmail.com*

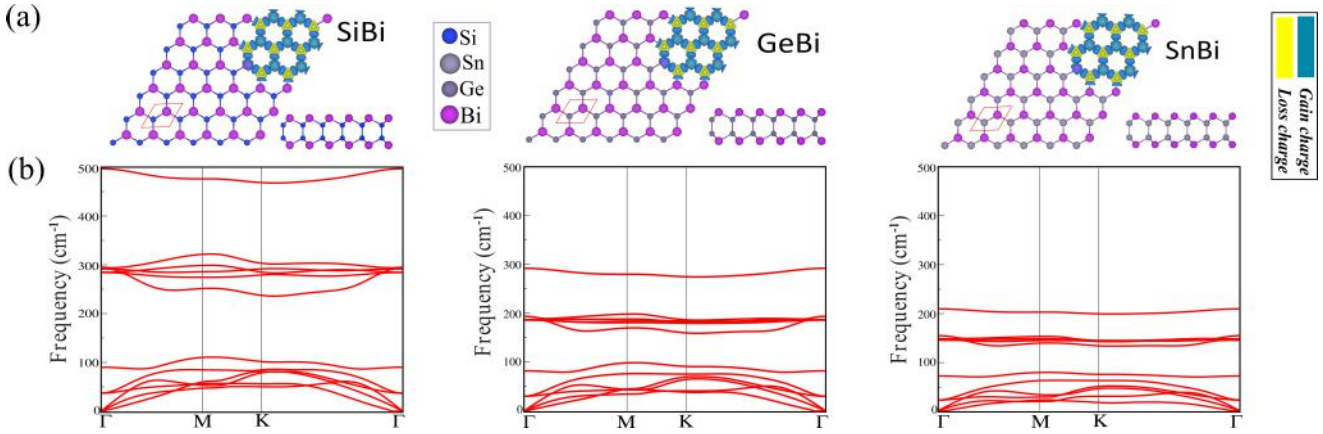

Fig. 1 (Color online) For the single-layers of XBi, (a) atomic structure and (b) phonon band dispersions. The primitive unit cell indicated by a red hexagonal and the difference charge density is shown in the same panel. The blue and yellow regions represent the charge accumulation and depletion, respectively.

lar cells, thermoelectric and optoelectronic energy conversion devices[32,33]. Thirdly, Bi-layered materials allow foreign ions to intercalate and to form multicomponent stable compounds without significant structural deformation due to their stable skeleton structure and a large interlayer space[34].

The another family members of 2D materials are binary compounds of a group IV element (Si,Ge,Sn) and group-III monochalcogenides with a representative chemical formula of MX (M=B, Ga, Al, In and X=O, S, Se, Te)[35–40] which have honeycomb lattice and that effectively consists of covalently bonded atomic planes are held together by van der Waals interactions as well as in TMDs have been extensively studied for decades due to their outstanding properties, such as remarkably high carrier mobility, p-type electronic response, sombrero-shape valence band edges, etc. To date, various MX systems such as InSe, GaS, GaSe, and GaTe have been experimentally realized and theoretical studies have reported a stable class of single-layer group IV monochalcogenides (YX, Y = Si, Ge, Sn and X = S, Se, and Te) that are semiconductors with wide band gaps. Due to above reason, we have selected silicon (Si), germanium (Ge), and tin (Sn) as chalcogen. It should be noted that anode materials based on the on Si, Ge, Sn show outstandingly high specific storage capacities of 4200, 1625, and 994 mAhg^{-1}, respectively, very appealing for the design of more efficient rechargeable batteries[41].

Motivated with the recent realization of 2D MX single-layers and their novel properties, here we study the vibrational, mechanical, electronic and thermal transport properties of XBi (X= Si, Ge, and Sn) single-layers by utilizing first principles calculations. Worthy to mention that these 2D lattices have been predicted by Ashton et al.[42] in 2016 and were also studied by Ozdamar et al.[43]. Nonetheless, results presented in our work further improve the understanding on the importance of the chemical composition and structural configuration of XBi (X= Si, Ge, and Sn) nanosheets and may hopefully guide experimental studies.

2 Method

We conducted density-functional theory (DFT) simulations using the projector augmented wave (PAW) and generalized gradient approximation (GGA) proposed by the Perdew-Burke-Ernzerhof (PBE) form[44,45] employing Vienna *ab-initio* Simulation Package (VASP)[46,47]. The vdW dispersion correction was applied via the DFT-D2 method of Grimme[48]. Spin-orbit-coupling (SOC) was taken into account for the electronic-band structure calculations. A kinetic energy cut-off of 600 eV was considered in DFT calculations for the plane-waves[49]. The hybrid functionals (HSE06)[50] with (SOC) were also taken into account as called HSE+SOC. The Brillioiun zone sampled by using a Γ-centered 16×16×1 *k*-point mesh for the unit cell. The geometries were optimized until the energy difference between two following steps were less than 10^{-5} eV, and maximum force on atoms was smaller than 10^{-3} eV Å^{-1}. A ∼20 Å vacuum was also applied along the sheet's normal direction to avoid the inaccuracies due to the interactions with monolayer images. The charge transfers are evaluated by the decomposition of charge density on the basis of Bader charge method[51]. The vibrational properties and the phonon dispersion relations were acquired via the small-displacement method using the PHONOPY code[52]. *Ab-initio* molecular dynamics (AIMD) simulations were also carried out to examine the thermal stability of XBi single-layers by using 4×4×1 super cell at room temperature (300 K) with total simulation time of 6 ps with 2 fs time steps.

3 Results and Discussions

In spite of reports of group IV-V compounds from experimental and theoretical studies, the lack of understanding on the hexagonal lattice of group IV-Bi, namely XBi where X=Sn, Si, or Ge, allow us to propose and investigate the stability of those single layer structures. Based on this fact, we systematically studied the structural, electronic, vibrational, mechanical, and thermal properties of 2D group IV-Bi binary single layers exhibiting hexagonal crystal structure. The quartic band dispersions of the investigated single layers are quite important for their thermoelectric performance.

3.1 Structure and Stability

The atomic structure of XBi single-layers consists of four three-coordinated X (Si, Ge and Sn) and four-fold coordinated Bi atoms in a hexagonal unit cell containing four atoms, as shown in Fig. 1(a). In the a single-layer structure 2-X layers are sandwiched between Bi-layers in the Bi-X-X-Bi order. The optimized lattice constants, $a = b$, are calculated to be 4.09, 4.15, and 4.35 Å, for SiBi, GeBi, and SnBi, respectively, which are slightly larger than those of Ga-monochalcogenides (3.58 and 3.75 Å for single-layers of GaS and GaSe structures, respectively). The bond lengths of d_1 (X-Bi) are found to be 2.69 Å (Si-Bi), 2.74 Å (Ge-Bi) and 2.90 Å (Sn-Bi), while the d_2 (X-X) are slightly smaller (2.31 Å (Si-Si), 2.43 Å (Ge-Ge) and 2.80 Å (Sn-Sn)). The charge density difference of XBi (X=Si, Ge, Sn) single-layers is shown in Fig. 1(a) in the same panel, in which yellow and blue color coding represent the charge depletion and accumulation, respectively. It is clear that Bi atoms are charged negatively and surrounded by X (Si, Ge and Sn) atoms that are positively charged, which reveal the charge transfer from X atoms to the connecting Bi atom. The difference charge density ($\Delta\rho$) is defined as:

$$\Delta\rho = \rho_{XBi} - \rho_X - \rho_{Bi} \quad (1)$$

where ρ_{XBi}, ρ_X and ρ_{Bi} represents the charge densities of the XBi and isolated atoms, respectively. Notice that each Bi atom gains about 0.04, 0.17 and 0.20 e from the adjacent Si, Ge and Sn atom in the SiBi, GeBi and SnBi single-layers, respectively. The charge redistribution is due to the different electro-negativities of 1.9 (Si), 2 (Ge), 1.96 (Sn) and 2.02 (Bi). The structural and electronic parameters of the XBi (X=Si, Ge, Sn) single-layers are listed in Table I. In order to calculate the cohesive energy E_{coh}, the used expression as follows:

$$E_{coh} = \frac{2E_X - 2E_{Bi} - E_{tot}}{n_{tot}} \quad (2)$$

where E_X and E_{Bi} represent the energies of isolated single X (Si, Ge and Sn) and Bi atoms, n_{tot} is the total number of unit cell, respectively; E_{tot} represents the total energy of the XBi single-layer. The cohesive energy of SiBi, GeBi and SnBi, are found to be 4.77, 4.47 and 4.23 eV/atom, respectively. As a matter of fact, the more negative values for cohesive energies confirm the more stability and thus the stability is higher for the lattices with a lighter X atom. We further analyze the formation energy of the considered structures using the formula below;

$$E_{for} = E_{bulk}(XBi)/layer - E^X_{bulk} - E^B_{bulk}i \quad (3)$$

where $E_{bulk}(XBi)$, E^X_{Bulk}, and $E^B_{Bulk}i$ represent the total energies of bulk form of XBi structure and that of the individual atoms. The calculated formation energies are 0.35, 0.54, and 0.59 eV for GeBi, SiBi, and SnBi single-layers, respectively. The positive formation energies indicate that the studied structures require finding an appropriate substrate for the growth, otherwise their synthesis from their native bulk lattices under ambient conditions are not probable.

The dynamical stability of XBi monolayers is investigated by calculating their phonon band dispersions through the whole BZ

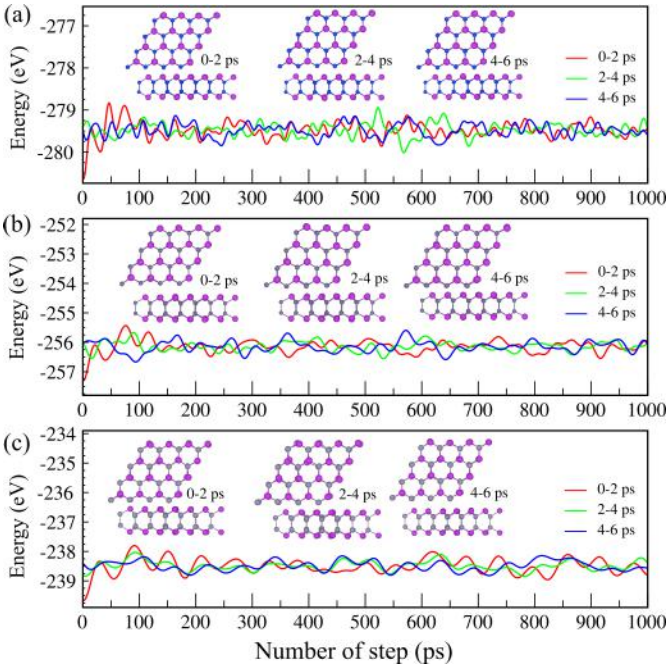

Fig. 2 (Color online) AIMD simulation of (a) SiBi, (b) GeBi and (c) SnBi single-layers. The snap shut of optimized structures are indicated in the inset.

which are presented in Figs. 1(b). Apparently, phonon branches are free from any imaginary frequencies indicating the dynamical stability of the structures. Similar to the case of single-layer InSe, which has the same symmetry and crystal structure with those of XBi, XBi single-layers exhibit three acoustic and nine optical phonon branches. Among nine of the optical branches, three of them are found to be non-degenerate out-of-plane vibrational modes while the remaining six are three different doubly-degenerate phonon modes. The calculated Raman spectra reveal

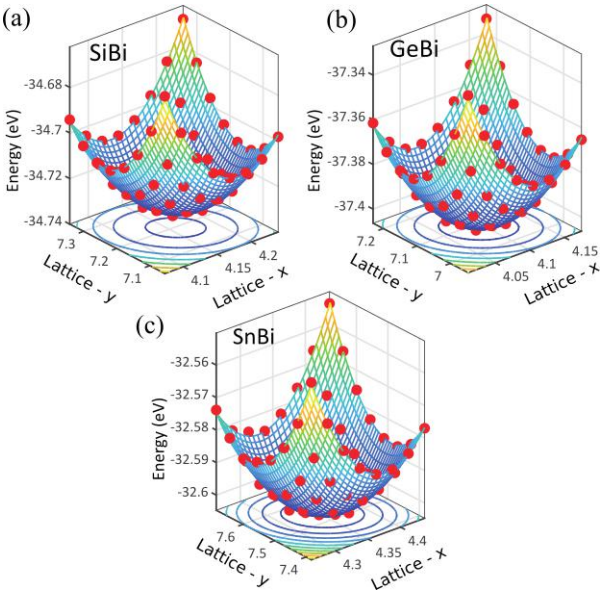

Fig. 3 Energy landscapes for the (a) SiBi, (b) GeBi and (c) SnBi single-layers.

Table 1 The calculated values for the optimized XBi single-layers: lattice constants *a*, bond distances (the bond length between X-Bi atoms d_{X-Bi} and X-X atoms d_{X-X}, where X=Si, Ge and Sn), bond angles between Bi-X-Bi atoms (θ_1) and Bi-X-X (θ_2), cohesive energy, charge differences (according to Bader analysis), electronic states (ES) are specified as metal (M) semiconductor (SC) and band gap energy (PBE / PBE+SOC / HSE+SOC)

	a (Å)	d_{X-Bi} (Å)	d_{X-X} (Å)	Δz (Å)	θ_1 (°)	θ_2 (°)	E_{coh} (eV/atom)	ΔQ (e)	ES (eV)	E_g (eV)
SiBi	4.09	2.69	2.31	4.89	98.94	118.63	4.65	0.04	SC	(0.71/0.25/0.65)
GeBi	4.15	2.74	2.43	5.08	98.65	118.86	4.32	0.17	M	(0.38/0/0)
SnBi	4.35	2.90	2.80	5.71	97.03	120.11	4.06	0.20	M	(0.30/0/0)

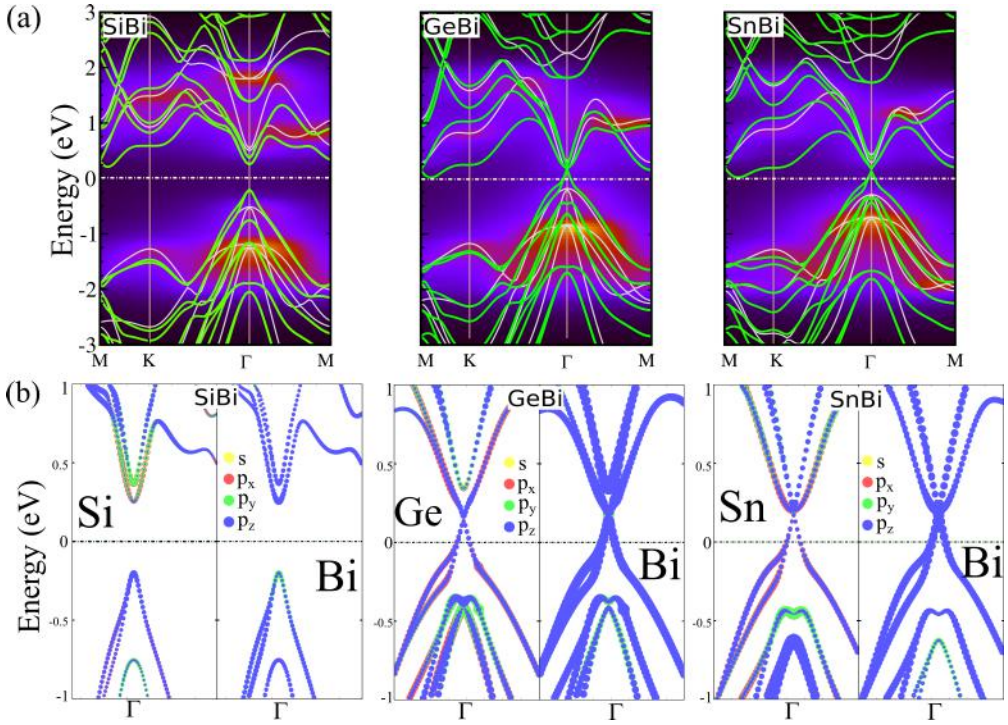

Fig. 4 (a) Intensity map of XBi (X=Si, Ge, Sn) single-layers with corresponding electronic band structure which overlayed by green line and (b) orbital resolved band structure with HSE+SOC of XBi single-layers.

that each single-layer structure exhibits three prominent Raman active modes which are described as follows: The highest frequency Raman active phonon mode has out-of-plane vibrational character. This mode is assigned to the opposite out-of-plane vibration of X-layers and Bi-layers, respectively. The frequencies of the mode are calculated to be 207, 291, and 496 cm^{-1} for single-layers SnBi, GeBi, and SiBi, respectively. In addition, the most prominent Raman active phonon mode is found to exhibit in-plane vibrational behavior. In this doubly-degenerate phonon mode, the X and Bi atoms vibrate out-of-phase in the in-plane directions that can be interpreted as the shear-like motion of X and Bi layers. The frequencies are found to be 146, 186, and 283 cm^{-1} for SnBi, GeBi, and SiBi, respectively. Moreover, each structure exhibits also an out-of-plane Raman active phonon mode which has relatively smaller intensity and frequency. The mode is assigned to the out-of-plane breathing-like vibration of top and bottom X-Bi sublayers. Its frequency is found to be 71, 82, and 89 cm^{-1} for SnBi, GeBi, and SiBi, respectively.

In addition, the thermal stability are examined by performing *ab-initio* molecular dynamics (AIMD) simulations using NVT ensemble with fixed particle number, volume and temperature. For the AIMD simulations, 32-atom supercell is used for each single-layer with a k-mesh of $4\times4\times1$. The dynamical investigations are started with the optimized structure of XBi single-layers at 0 K and discussed in the stability of XBi single-layers section. We have further extend our calculations to the thermal stability at room temperature. During the simulations, temperature is kept at 300 K, the fluctuations of total energy and evolutions of XBi atomic structures during the simulations are shown in Figs. 2(a-c). The time step was set to 2 fs and, to reach a total simulation time of 6 ps, 1000 steps were realized three times. Due to the large size of the cell, all the calculations were performed with each 2 ps. The structure snapshots are taken at the end of the each simulation in every 2 ps. As can be seen in Fig. 2, none of the single-layers undergo structural reconstruction even around 300 K indicating the thermal stability of each single-layer. The variation of total energy per atom is 1 eV which is in the acceptable range similar to many studies in the literature. In addition, as the X atoms changes from Si to Sn, the single-layer structure displays in-plane buckling with increasing temperature due to different X-Bi and

Bi-Bi bond formations. It can be concluded that XBi single-layers exhibit thermal stability around the room temperature.

Another analysis to test the stability of the considered material is the investigation of the mechanical properties. For this purpose, we firstly change the unitcells of the XBi structures to the rectangular cell and applied sequential uniaxial strains. The applied maximum strain ratio is $\mp 2\%$ of the relevant lattice parameter of the rectangular cells. Obtained energies versus lattice parameters (energy landscape) are given in Figs. 3(a-c). To calculate the in-plane stiffness[53] we used $C_{x,y}=(1/A)\partial E_T^2/\partial \varepsilon_{x,y}^2$ and to find Poisson's ratio we used $\nu_{x,y}=\varepsilon_y/\varepsilon_x$ equations. In here, A defined the unitcell area, E_T is for the total energy per cell of the XBi structure, and the applied uniaxial strain along the x,y axis is defined as $\varepsilon_{x,y}$. Because of equivalent in-plane lattice constants of the XBi structures, we found that $C_x = C_y$ and $\nu_{xy} = \nu_{yx}$. The calculated in-plane stiffness values are 76.96, 64.13 and 45.72 J/m^2 for SiBi, GeBi and SnBi, respectively while the obtained Poisson's ratio values are 0.279, 0.295, and 0.290. These results indicate that in-plane stiffness of the XBi structures get smaller while going from SiBi to SnBi. However, these in-plane stiffness values are larger than their individual components such as Silicene, Germanene, Stanene and Bismuthene,[54–56] while these numbers are almost equal to that of many transition metal dichalcogenides.[57,58]

3.2 Electronic Properties

The intensity map band structure of XBi single-layers is shown in Fig. 4(a) which overlayed with its electronic band structure with considering spin orbital coupling (SOC). XBi single-layers exhibit semiconducting behavior without SOC effects and the calculated band gaps are 0.71, 0.38 and 0.30 eV for SiBi, GeBi and SnBi, respectively. However, inclusion of SOC shows that only the SiBi single-layer is a semiconductor with an indirect band gap of 0.25 eV under PBE+SOC functional. In addition, the conduction band minimum (CBM) of SiBi resides between the $M-K$ points while the valence band maximum (VBM) lies at the Γ-point. The HSE06 functional is also used to evaluate the energy band gap. We see that the HSE06 approach does not change the sort of indirect band gap however, it gives rise to an increase of the band gap to 0.65âĂŕeV. The calculated electron effective mass along Γ $\longrightarrow$ K (M) is 0.15 (0.29) m_e^*, whereas the hole effective mass is estimated to be -0.1 and -0.16 m_e^* along Γ $\longrightarrow$ K and Γ $\longrightarrow$ M, respectively. These estimated light effective masses for the electron and hole confirm high carriers mobility in these novel nanosheets. In contrast SiBi single-layer, we find that the GeBi and SnBi single-layers show a metallic characteristic. To better examine the contribution of different orbitals to the electronic states and the bonding characteristics of XBi single-layers, we carry out the calculations of the orbital-resolved band structure as shown in Fig. 4(b) It is conspicuous that the states near the Fermi energy shows contributions from p orbitals of X and Bi atoms. It is clear that X and Bi atoms p_z orbitals contributions are much higher than that from $p_{x,y}$-orbitals. The fact that the p_z-orbitals are dominant is caused by the sp^3-like bond of X and the sp^2-like bond of Bi forming the SiBi single-layer. In addition, the contribution of p_z-orbitals can also allow the surface oxidation of the studied structures. From Fig. 2(b) is clearly seen that the metallicity of GeBi and SnBi single-layers mainly are composed of the p_z orbitals of Bi atom, while the contribution of Ge or Sn atom orbitals do not contribute.

3.3 Thermoelectric Properties

In order to estimate the thermoelectric properties of the XBi single-layers, the semiclassical Boltzmann transport theory (BTT) within the constant relaxation time approximation and the rigid band approach as implemented in the BoltzTraP2 code was used.[59,60] By using this package and based on the electronic structure, the Seebeck coefficient (S), electrical conductivity (σ) and power factor ($S^2\sigma$) are all calculated. Obtained results are given with respect to relaxation time τ, and it depends on the material properties, however, in this study the relaxation time is fixed to 10 fs ($\tau = 10^{14}$s) as taken by many studies.[61,62] As seen in Fig. 5, we calculated S, σ and $S^2\sigma$ for various temperature from 250K to 500K for every 50K steps using the BoltzTraP2 code. It should be noted, we only give the maximum value of the Seebeck coefficient and corresponding (σ) value for the selected temperatures. For bare XBi single-layers, we obtained a high Seebeck coefficient and the calculated largest S value is for SnBi single-layer for all considered temperatures while the smallest S value is for SiBi single-layer. With the increasing of the temperature from 250K to 500K the S values of the XBi single-layers decrease more than half of the initial values. Electrical conductivity of XBi single-layers start to increase after 400K and the σ of SiBi suddenly get a high value after 450K. The efficiency of thermoelectric materials is given by the dimensionless figure of merit $ZT = S^2\sigma T/\kappa$, where T is the absolute temperature and κ is the thermal conductivity, which is the sum of contributions from electron (κ_e) and lattice (κ_l) parts. High ZT can obtain by a high power factor and a low κ value. For this purpose we calculated the power factor of the XBi structures. As can be seen in the right part of the Fig. 5, curve of the $S^2\sigma$ is similar to the σ curve due to dominant increasing of the σ. We note that the calculated κ_e values are very low as needed for high ZT. Notably, in order to find an exact value for the ZT, the lattice thermal conductivity should be determined by the behavior of phonon transport in the XBi single-layers. Moreover, in terms of the electronic features, in the case of doping, either $p-$ or $n-$type, semiconducting nature of single-layer SiBi will be affected in terms of the Fermi energy level. It can be expected that the doping amount either increase or decrease the thermoelectric power up to certain value of doping amount. Therefore, the effect doping on the thermoelectric properties can also be taken into account.

Scattering region between the acoustic and optical phonon branches is important to determine the lattice thermal conductivity, large scattering region will lower the heat flux, and thus result in lower contribution of the thermal conductivity from phonons. As can be seen from the phonon structures of the XBi single-layers (see Fig. 1(b)), frequency of the optical modes reduce while going from SiBi to SnBi and lowest optical branches of the XBi structures get closer to the highest acoustic branches which results in the narrower scattering region. The largest scattering region of

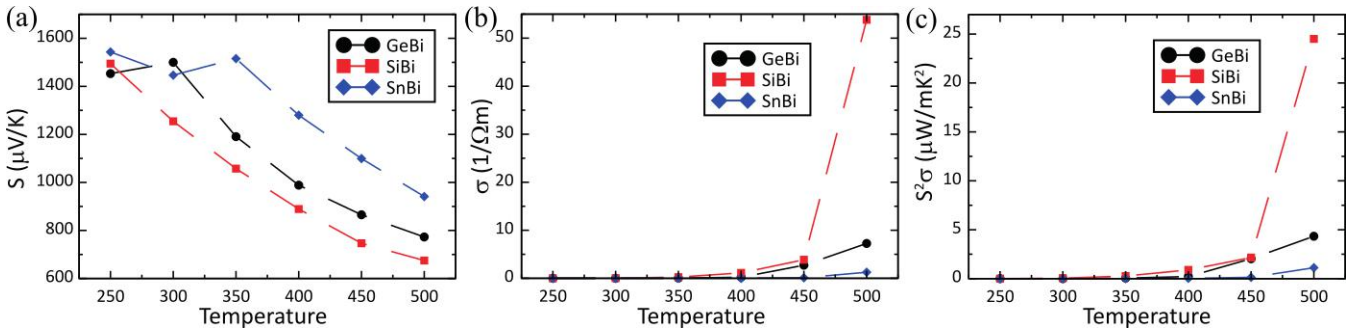

Fig. 5 (Color online) The calculated Seebeck coefficient (S), electrical conductivity σ and power factor ($S^2\sigma$) of XBi single-layers for various temperatures from 250K to 500K.

the SnBi may give the lowest κ_l value and it has relatively high ZT value than other XBi single-layers.

3.4 Substrate Effect

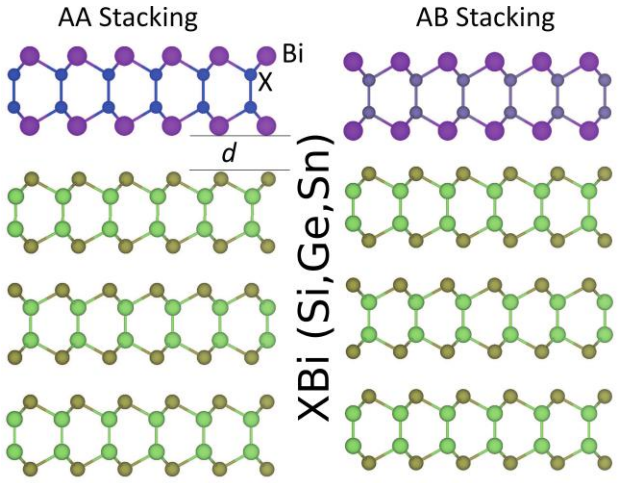

Fig. 6 Side views of the XBi single-layers on various bulk structures. Two stacking types (AA stacking and AB stacking) considered according to top layer of the considered bulk materials.

As it is known, in order to synthesize a single-layer structure, a suitable substrate is of importance. There are two most important restrictions which should be considered. First one is the lattice mismatch ratio between the substrate and the material to be synthesized, second is the interaction between the two materials that should be very weak as vdW binding to avoid the structural reconstructions on the single-layer structure. By considering these two condition we try to find suitable substrates for XBi single-layers. For this purpose we focused on the bulk materials which have similar atomic structure with XBi materials. The calculated lattice parameters are a=b=4.09 Å and c=16.67 Å for bulk GaTe, a=b=4.01 Å and c=16.92 Å for bulk InSe and a=b=4.25 Å and c=17.69 Å for bulk InTe. If we cut the bulk materials from the (001) plane, the lattice mismatch ratio between the unitcells of the bulk and XBi materials becomes less than 2% which is acceptable ratio to growth XBi on these selected bulk materials. According to the lattice mismatch, GeBi placed on (001)GaTe, SiBi placed on both of (001)GaTe and (001)InSe and SnBi placed on (001)InTe substrates. Each XBi single-layers placed initially 3Å above on the selected substrates and to avoid the computational cost three layers are selected for the substrates and all atoms released to geometric optimization. To determine the favorable stacking orientation we considered two stacking types as illustrated in Fig. 6. The optimized structures revealed that AB stacking type is energetically approximately 0.20 eV more favorable than AA stacking order for the all structures. The calculated inter-layer energy between XBi and bulk materials for AB stacking types are -0.400 eV for GeBi@GaTe, -0.351 eV for SiBi@GaTe and -0.289 eV for SiBi@InSe and -0.409 for SnBi@InTe. These inter-layer energies indicate that the interaction between XBi and substrates can consider as vdW bonding, these results are verified by the Bader charge analysis, calculated charge transfer between the layers are in the range of 0.04-0.07 e. At the end of the optimization the normal distance in z-axis (d) between XBi and substrates are in the range of 3.10-3.40 Å. These results show that obtained properties for XBi single-layers will not effect much from these selected substrates due to physisorption of XBi single-layers and almost no net charge transfer between the XBi and substrates. In addition, the single-layer on top of the substrates are relaxed at 400 K for 4 ps with *ab-initio* molecular dynamics simulations and it is shown that the single-layers do not go under structural deformations. So, based on these results we can conclude that our results of free-standing XBi outlined in the previous sections can be useful for experimentalists who attempts to synthesize these materials.

4 Conclusion

In this study, we investigate the electronic, mechanical, thermoelectric properties of single-layer XBi (X=Ge, Si, or Sn) structures by first-principles calculations. Dynamical stability of each single-layer was verified in terms of their phonon band dispersions while the *ab-initio* molecular dynamics simulations revealed the thermal stability of each single-layer structure. Raman spectra calculations indicated that three structures exhibit similarities in terms of their Raman active phonon modes with distinctive phonon frequencies. Electronic band structures showed that single-layer SiBi is an indirect band gap semiconductor while GeBi and SnBi exhibit metallic behaviors. Moreover, the calculated linear-elastic parameters indicated the quite soft nature of the proposed single-layers which makes them suitable for nanoelastic applications.

Our results for the thermoelectric properties of single-layer XBi revealed the high potential of SiBi in terms of its thermoelectric coefficient which increases at high temperatures. Furthermore, we investigated the possible substrate effect on the structural formation of XBi single-layers. It was shown that either with their small lattice mismatch or weak substrate-XBi interaction, layered GaTe, InSe, and InTe are shown to be potential substrates for experimental realizations of single-layer XBi structures. Overall, it was shown that single-layer XBi structures can be alternative, stable 2D single-layers with their varying electronic and thermoelectric properties.

5 Conflicts of interest

The authors declare that there are no conflicts of interest regarding the publication of this paper.

6 ACKNOWLEDGMENTS

This work was supported by the National Research Foundation of Korea(NRF) grant funded by the Korea government (MSIT) (NRF-2015M2B2A4033123). Computational resources were provided by the Flemish Supercomputer Center (VSC). M.Y. is supported by the Flemish Science Foundation (FWO-Vl) by a postdoctoral fellowship. B.M. appreciates the funding by the Deutsche Forschungsgemeinschaft (DFG, German Research Foundation) under GermanyâĂŹs Excellence Strategy within the Cluster of Excellence PhoenixD (EXC 2122, Project ID 390833453).

References

1 K. S. Novoselov, A. K. Geim, S. V. Morozov, D. Jiang, Y. Zhang, S. V. Dubonos, I. V. Grigorieva and A. A. Firsov, *Sci.*, 2004, **306**, 666–669.

2 A. K. Geim and K. S. Novoselov, in *A. K. Geim and K. S. Novoselov*, World Scientific, 2007, vol. 306, pp. 183–191.

3 C. Lee, X. Wei, J. W. Kysar and J. Hone, *Sci.*, 2008, **321**, 385–388.

4 S. Cahangirov, M. Topsakal, E. Akturk, H. Sahin and S. Ciraci, *Phy. Rev. Lett.*, 2009, **102**, 236804.

5 B. Feng, O. Sugino, R.-Y. Liu, J. Zhang, R. Yukawa, M. Kawamura, T. Iimori, H. Kim, Y. Hasegawa, H. Li *et al.*, *Phy. Rev. Lett.*, 2017, **118**, 096401.

6 F.-f. Zhu, W.-j. Chen, Y. Xu, C.-l. Gao, D.-d. Guan, C.-h. Liu, D. Qian, S.-C. Zhang and J.-f. Jia, *Nat. Mater.*, 2015, **14**, 1020–1025.

7 A. J. Mannix, X.-F. Zhou, B. Kiraly, J. D. Wood, D. Alducin, B. D. Myers, X. Liu, B. L. Fisher, U. Santiago, J. R. Guest *et al.*, *Sci.*, 2015, **350**, 1513–1516.

8 X. Xu, W. Yao, D. Xiao and T. F. Heinz, *Nat. Phys.*, 2014, **10**, 343–350.

9 M. Chhowalla, H. S. Shin, G. Eda, L.-J. Li, K. P. Loh and H. Zhang, *Nat. Chem.*, 2013, **5**, 263.

10 S. Tongay, J. Zhou, C. Ataca, K. Lo, T. S. Matthews, J. Li, J. C. Grossman and J. Wu, *Nano lett.*, 2012, **12**, 5576–5580.

11 L. Banszerus, M. Schmitz, S. Engels, J. Dauber, M. Oellers, F. Haupt, K. Watanabe, T. Taniguchi, B. Beschoten and C. Stampfer, *Sci. Adv.*, 2015, **1**, e1500222.

12 D. G. Papageorgiou, I. A. Kinloch and R. J. Young, *Prog. Mater. Sci.*, 2017, **90**, 75–127.

13 Y. Liu, R. Cheng, L. Liao, H. Zhou, J. Bai, G. Liu, L. Liu, Y. Huang and X. Duan, *Nat. Commun.*, 2011, **2**, 1–7.

14 G. Lu, K. Yu, Z. Wen and J. Chen, *Nanoscale*, 2013, **5**, 1353–1368.

15 H. Liu, A. T. Neal, Z. Zhu, Z. Luo, X. Xu, D. Tomanek and P. D. Ye, *ACS nano*, 2014, **8**, 4033–4041.

16 P. Vogt, P. De Padova, C. Quaresima, J. Avila, E. Frantzeskakis, M. C. Asensio, A. Resta, B. Ealet and G. Le Lay, *Phys. Rev. Lett.*, 2012, **108**, 155501.

17 M. Davila, L. Xian, S. Cahangirov, A. Rubio and G. Le Lay, *N. J. Phys.*, 2014, **16**, 095002.

18 C.-C. Liu, H. Jiang and Y. Yao, *Phys. Rev. B*, 2011, **84**, 195430.

19 L. Cheng, H. Liu, X. Tan, J. Zhang, J. Wei, H. Lv, J. Shi and X. Tang, *The J. Phys. Chem. C*, 2014, **118**, 904–910.

20 L. Cheng, C. Zhang and Y. Liu, *Phys. Rev. Lett.*, 2020, **125**, 177701.

21 A. Bafekry, F. Shojai, D. M. Hoat, M. Shahrokhi, M. Ghergherehchi and C. Nguyen, *RSC Adv.*, 2020, **10**, 30398–30405.

22 L. Cheng, H. J. Liu, J. Zhang, J. Wei, J. H. Liang, P. H. Jiang, D. D. Fan, L. Sun and J. Shi, *Phys. Chem. Chem. Phys.*, 2016, **18**, 17373–17379.

23 T. V. Vu, C. V. Nguyen, H. V. Phuc, A. A. Lavrentyev, O. Y. Khyzhun, N. V. Hieu, M. M. Obeid, D. P. Rai, H. D. Tong and N. N. Hieu, *Phys. Rev. B*, 2021, **103**, 085422.

24 A. Bafekry, F. Shojaei, M. M. Obeid, M. Ghergherehchi, C. Nguyen and M. Oskouian, *RSC Adv.*, 2020, **10**, 31894–31900.

25 H. T. T. Nguyen, V. T. T. Vi, T. V. Vu, N. V. Hieu, D. V. Lu, D. P. Rai and N. T. T. Binh, *RSC Adv.*, 2020, **10**, 44785–44792.

26 X. Liu, S. Zhang, S. Guo, B. Cai, S. A. Yang, F. Shan, M. Pumera and H. Zeng, *Chem. Soc. Rev.*, 2020, **49**, 263–285.

27 K. Xu, L. Wang, X. Xu, S. X. Dou, W. Hao and Y. Du, *Energy Storage Mater.*, 2019.

28 X. Li, Y. Sun, T. Xiong, G. Jiang, Y. Zhang, Z. Wu and F. Dong, *J. catalysis*, 2017, **352**, 102–112.

29 R. He, D. Xu, B. Cheng, J. Yu and W. Ho, *Nanoscale Horizons*, 2018, **3**, 464–504.

30 Z. Xu, K. Xu, H. Feng, Y. Du and W. Hao, *Sci. Bulletin*, 2018, **63**, 465–468.

31 H. Feng, Y. Du, C. Wang and W. Hao, *Current Opinion in Green and Sustainable Chemistry*, 2017, **6**, 93–100.

32 R. A. Schlitz, F. G. Brunetti, A. M. Glaudell, P. L. Miller, M. A. Brady, C. J. Takacs, C. J. Hawker and M. L. Chabinyc, *Adv. Mater.*, 2014, **26**, 2825–2830.

33 F. Zhang and C.-a. Di, *Chem. Mater.*, 2020.

34 S. Zhang, M. Xie, F. Li, Z. Yan, Y. Li, E. Kan, W. Liu, Z. Chen and H. Zeng, *Ange. Chem. Inter.*, 2016, **55**, 1666–1669.

35 L. Xu, M. Yang, S. J. Wang and Y. P. Feng, *Phys. Rev. B*, 2017, **95**, 235434.

36 C. Barreteau, B. Michon, C. Besnard and E. Giannini, *J. Crystal Growth*, 2016, **443**, 75–80.

37 S. Demirci, N. Avazlı, E. Durgun and S. Cahangirov, *Phys. Rev. B*, 2017, **95**, 115409.

38 J.-H. Lin, H. Zhang, X.-L. Cheng and Y. Miyamoto, *Phys. Rev. B*, 2017, **96**, 035438.

39 A. Mogulkoc, Y. Mogulkoc, S. Jahangirov and E. Durgun, *J. Phys. Chem. C*, 2019, **123**, 29922–29931.

40 İ. Eren, S. Ozen, Y. Sozen, M. Yagmurcukardes and H. Sahin, *J. Phys. Chem. C*, 2019.

41 W. Li, X. Sun and Y. Yu, *Small Methods*, 2017, **1**, 1600037.

42 M. Ashton, S. B. Sinnott and R. G. Hennig, *Appl. Phys. Lett.*, 2016, **109**, 192103.

43 M. N. C. K. S. G. K. B. K. B. Ozdamar, G. Ozbal and H. Sevincli, *Phys. Rev. B*, 2018, **98**, 045431.

44 J. P. Perdew, K. Burke and M. Ernzerhof, *Phys. Rev. Let.*, 1996, **77**, 3865.

45 J. P. Perdew, K. Burke and M. Ernzerhof, *Phys. Rev. Let.*, 1996, **77**, 3865.

46 G. Kresse and J. Hafner, *Phys. Rev. B*, 1993, **47**, 558.

47 G. Kresse and J. Furthmuller, *Phys. Rev. B*, 1996, **54**, 11169.

48 S. Grimme, *J. Comput. Chem.*, 2006, **27**, 1787–1799.

49 G. Kresse and D. Joubert, *Phys. Rev. B*, 1999, **59**, 1758.

50 J. Paier, M. Marsman, K. Hummer, G. Kresse, I. C. Gerber and J. G. Angyan, *J. Chem. Phys.*, 2006, **124**, 154709.

51 G. Henkelman, A. Arnaldsson and H. Jonsson, *Comput. Mater. Sci.*, 2006, **36**, 354–360.

52 D. Alfe, *Comput. Phys. Commun.*, 2009, **180**, 2622–2633.

53 M. Topsakal, S. Cahangirov and S. Ciraci, *Appl. Phys. Lett.*, 2010, **96**, 091912.

54 H. Sahin, S. Cahangirov, M. Topsakal, E. Bekaroglu, E. Akturk, R. T. Senger and S. Ciraci, *Phys. Rev. B*, 2009, **80**, 155453.

55 E. Akturk, O. U. Akturk and S. Ciraci, *Phys. Rev. B*, 2016, **94**, 014115.

56 F. Ersan, E. Akturk and S. Ciraci, *Phys. Rev. B*, 2016, **94**, 245417.

57 Z. Kahraman, A. Kandemir, M. Yagmurcukardes and H. Sahin, *J. Phys. Chem. C*, 2019, **123**, 4549–4557.

58 F. Ersan, S. Cahangirov, G. Gokoglu, A. Rubio and E. Akturk, *Phys. Rev. B*, 2016, **94**, 155415.

59 G. K. Madsen, J. Carrete and M. J. Verstraete, *Comput. Phys. Commun.*, 2018, **231**, 140–145.

60 G. K. Madsen and D. J. Singh, *Comput. Phys. Commun.*, 2006, **175**, 67–71.

61 S. Sarikurt, D. Cakir, M. Keceli and C. Sevik, *Nanoscale*, 2018, **10**, 8859–8868.

62 G. Ding, G. Y. Gao and K. L. Yao, *J. Phys. D: Appl. Phys.*, 2015, **48**, 235302.